



**HAL**  
open science

# Effects of different coronal hole geometries on simulations of the interaction between coronal waves and coronal holes

I. Piantschitsch, J. Terradas, E. Soubrie, S. G. Heinemann, S. J. Hofmeister,  
R. Soler, M. Temmer

## ► To cite this version:

I. Piantschitsch, J. Terradas, E. Soubrie, S. G. Heinemann, S. J. Hofmeister, et al.. Effects of different coronal hole geometries on simulations of the interaction between coronal waves and coronal holes. *Astronomy & Astrophysics*, 2024, 687, 10.1051/0004-6361/202348003 . insu-04843868

**HAL Id: insu-04843868**

**<https://insu.hal.science/insu-04843868v1>**

Submitted on 18 Dec 2024



**HAL** is a multi-disciplinary open access archive for the deposit and dissemination of scientific research documents, whether they are published or not. The documents may come from teaching and research institutions in France or abroad, or from public or private research centers.

L'archive ouverte pluridisciplinaire **HAL**, est destinée au dépôt et à la diffusion de documents scientifiques de niveau recherche, publiés ou non, émanant des établissements d'enseignement et de recherche français ou étrangers, des laboratoires publics ou privés.



Distributed under a Creative Commons Attribution 4.0 International License

# Effects of different coronal hole geometries on simulations of the interaction between coronal waves and coronal holes

I. Piantschitsch<sup>1,2,3</sup>, J. Terradas<sup>1,2</sup> , E. Soubrie<sup>2,4</sup>, S. G. Heinemann<sup>5</sup>, S. J. Hofmeister<sup>6</sup>,  
R. Soler<sup>1,2</sup>, and M. Temmer<sup>3</sup> 

<sup>1</sup> Departament de Física, Universitat de les Illes Balears (UIB), Palma 07122, Spain  
e-mail: [isabell.piantschitsch@uib.es](mailto:isabell.piantschitsch@uib.es)

<sup>2</sup> Institute of Applied Computing & Community Code (IAC<sup>3</sup>), UIB, Palma, Spain

<sup>3</sup> Institute of Physics, University of Graz, Universitätsplatz 5, 8010 Graz, Austria

<sup>4</sup> Institut d'Astrophysique Spatiale, CNRS, Univ. Paris-Sud, Université Paris-Saclay, Bât. 121, 91405 Orsay, France

<sup>5</sup> Department of Physics, University of Helsinki, PO Box 64, 00014 Helsinki, Finland

<sup>6</sup> Columbia University, 116th and Broadway, New York, NY 10027, USA

Received 18 September 2023 / Accepted 5 March 2024

## ABSTRACT

The geometry of a coronal hole (CH) affects the density profile of the reflected part of an incoming global coronal wave (CW). In this study, we perform for the first time magnetohydrodynamic (MHD) simulations of fast-mode MHD waves that interact with CHs of different geometries, such as circular, elliptic, convex, and concave shapes. We analysed the effect of these geometries on the density profiles of the reflected waves, and we generated the corresponding simulation-based time-distance plots. Within these time-distance plots, we determined regions that exhibit specific density features, such as large reflected density amplitudes. In a further step, these interaction features can be compared to actual observed CW–CH interaction events, which will enable us to explain interaction parameters of the observed interaction events, such as the density structure of the reflected wave. These parameters are usually difficult to understand comprehensively based on an analysis of the measurements alone. Moreover, we show that the interaction between a concave CH and CWs, whose density profile includes an enhanced as well as a depleted wave part, can lead to reflected density amplitudes that are more than twice larger than the incoming density amplitudes. Another effect of the interplay between the constructive and destructive interference of the reflected wave parts is a strongly depleted region in the middle of the CW–CH interaction process. In addition, we show that the choice of the path that is used to generate the time-distance plots is important and that this choice affects the interpretation of the CW–CH interaction results.

**Key words.** magnetohydrodynamics (MHD) – waves – Sun: corona

## 1. Introduction

The interactions between global coronal waves (CWs) and coronal holes (CHs) can be studied either by analysing the corresponding observations and measuring the involved parameters (Kienreich et al. 2013; Olmedo et al. 2012; Gopalswamy et al. 2009; Liu et al. 2019; Chandra et al. 2022; Zhou et al. 2022; Mancuso et al. 2021), or by performing numerical magnetohydrodynamic (MHD) simulations (Afanasyev & Zhukov 2018; Piantschitsch et al. 2017, 2018a,b, 2020) and by thus trying to mimic the actual observed interaction events. Additionally, there is the possibility to directly compare the observational measurements with the numerical results and to therefore obtain an even more comprehensive insight into the whole interaction process. This study is the second in a series of papers that aims to perform this direct comparison and to eventually reconstruct actual observed CW–CH interaction events. As a continuation of the first paper, in which the emphasis was on the initial density profile of the incoming wave (Piantschitsch et al. 2023), the current study focuses on the geometry of the CH and its effect on the CW–CH interaction features.

Why is it important to study these interaction features in the first place? The interaction between CWs and CHs results, among other effects, in the formation of reflected, refracted, and

transmitted waves (collectively: secondary waves). These interaction features have been confirmed by observations (Long et al. 2008; Gopalswamy et al. 2009; Kienreich et al. 2013; Liu et al. 2019; Olmedo et al. 2012; Veronig et al. 2006) as well as by numerical simulations (Piantschitsch et al. 2017, 2018a,b; Afanasyev & Zhukov 2018). One reason for the relevance of studying these interactions is the still lacking explanation for ambiguous phase-speed measurements of secondary waves (Gopalswamy et al. 2009; Podladchikova et al. 2019). Another motivation for this study is the fact that CW–CH interaction features can provide crucial information about the characteristics of CHs themselves, in particular, about their boundaries, and hence, about the prediction of high-speed solar wind streams (Riley et al. 2015; Hofmeister et al. 2022). In addition to this, recent studies showed that simulations of the interaction of CWs and CHs might be able to explain certain puzzling features in time-distance plots of actual observed interaction events (Piantschitsch et al. 2023).

Which parameters are of importance in the interaction process? The two main protagonists in the interaction process are obviously CHs and CWs. CWs are defined as large-scale propagating disturbances in the corona, and they can be observed throughout the entire solar surface. They have been

called “EIT waves” because they were directly observed for the first time by the Extreme-ultraviolet Imaging Telescope (EIT; [Delaboudinière et al. 1995](#)) on board the Solar and Heliospheric Observatory ([Domingo et al. 1995](#); [Thompson et al. 1998](#)). These propagating coronal disturbances are often also referred to as extreme-UV (EUV) waves or coronal bright fronts, and they are commonly associated with energetic eruptions such as coronal mass ejections (CMEs; see e.g. [Vršnak & Lulić 2000](#)). The amplitude of a CW is a crucial factor for the analysis of the interaction of CWs and CHs. The amplitude is commonly expressed as a compression factor with a value of about 1.1 or lower for CWs with moderate speed ([Warmuth 2015](#)) (which was also used in the setup for this study), but it can reach compression factors of up to 1.5 that are visible even in the lower chromosphere. They are then called Moreton waves ([Moreton & Ramsey 1960](#)). This density amplitude parameter is derived from intensity measurements of CWs ([Muhr et al. 2011](#)), together with the relation between intensity and density, which can roughly be described as  $\rho/\rho_0 \sim \sqrt{I/I_0}$  (see [Warmuth 2015](#)).

Coronal holes are the second main component in the interaction process and are the focus of this study. CHs are low-density low-temperature weak magnetic field regions that are known as the primary source of fast solar wind streams. Through interaction with the ambient slow solar wind, they result in stream interaction regions and may cause geomagnetic effects ([Cranmer 2009](#)). The CH parameters, such as their area, boundary geometry, and the longitudinal and latitudinal extent, affect the predictions of high-speed solar wind streams ([Hofmeister et al. 2022](#); [Samara et al. 2022](#); [Riley et al. 2015](#)). The on-disk CHs that have been studied so far are separated into those at the poles and those located in the disk center ([Heinemann et al. 2020](#)). While polar CHs typically cover quite large areas, CHs in the disk center, which tend to appear in more active periods of the solar cycle ([Cranmer 2009](#)), are smaller. Some CHs at lower latitudes can exhibit long convex and concave boundaries as well, but many of their boundaries are quite often similar to circular and elliptic shapes.

Which parameters are available to describe CHs? Several parameters that characterise CHs have been measured and analysed in increasing detail within the past decade. The most relevant parameter for our simulations is the density inside a CH, which is found to drop by 30% to 70% on average with respect to the quiet Sun ([Del Zanna & Bromage 1999](#); [Del Zanna & Mason 2018](#); [Saqri et al. 2020](#); [Heinemann et al. 2021](#)). Another crucial parameter is the width of the coronal hole boundary (CHB). It provides information about whether there is a sharp density drop or a smooth gradient from the quiet Sun to the interior of the CH ([Heinemann et al. 2019](#)). The parameter which we focus on in this study is the shape of the CHB. It has played an increasingly important role in recent studies. The detection of CHBs has become a crucial topic on its own and has led to the development of several different methods that aim to improve this detection, such as the collection of analysis tools for coronal holes (CATCH; [Heinemann et al. 2019](#)), which is a threshold-based extraction method, and the multi-channel coronal hole detection method developed by [Jarolim et al. \(2021\)](#), which is based on convolutional neural networks. These and other CHB detection methods have recently been compared with regard to their observational uncertainty ([Linker et al. 2021](#); [Reiss et al. 2021](#)).

How can we compare the simulation results to the observational measurements? The parameters involved in the observed interaction process are hard to derive unambiguously because they are derived from intensity measurements and are based on

the temperature-dependent filtergrams in the EUV. The analysis of the interaction parameters, such as the phase speed of the secondary waves, still mostly relies on studying the corresponding time-distance plots (e.g., [Liu et al. 2019](#); [Chandra et al. 2022](#); [Zhou et al. 2022](#); [Mancuso et al. 2021](#)). In this study, we create time-distance plots based on the simulations to analyse the behaviour of the secondary waves in a way analogous to what is commonly done for observations. These results, combined with the results from [Piantschitsch et al. \(2023\)](#), are used in a next step to partially reconstruct observational time-distance plots, and in this way, to directly compare the wave features from observations to those generated by simulations.

The effect of the CH density and the initial density amplitude of the incoming wave have mostly been studied in simulations of CW–CH interaction events so far ([Afanasyev & Zhukov 2018](#); [Piantschitsch et al. 2017, 2018a,b](#)). Other theoretical studies have taken into account the incident angle of the incoming wave and have provided analytical terms for estimating the density amplitude and phase speed of reflected and transmitted waves of a CW–CH interaction ([Piantschitsch et al. 2020](#); [Piantschitsch & Terradas 2021](#)). Very recently, the effect of a realistic density profile of an incoming wave, including an enhanced as well as a depleted wave part, has been studied for the first time ([Piantschitsch et al. 2023](#)). However, the geometry of the CH, which is a crucial parameter in the interaction process, has not been included in any MHD simulation so far.

The aim of this paper is to study the effect of the CH geometry on the interaction between CWs and CHs. The CH geometry and the resulting interaction effects are analysed especially with regard to understanding and reconstructing observational time-distance plots. By generating the simulation-based time-distance plots and comparing them directly to those based on observations, we aim to provide a tool for deriving parameters from actual observed interaction events, which are typically quite difficult to obtain directly from the measurements.

The paper is structured in the following way: Sect. 2 is dedicated to the initial setup of the simulations and to the description of the numerical scheme. In addition, some examples of CHs in observations illustrate the motivation for the setup. In Sect. 3, we present the simulation results of a CW that interacts with the different CH geometries, and we analyse the temporal evolution of the different corresponding 2D density structures. Section 4 is dedicated to the analysis of the simulation-based time-distance plots and to identifying different representative areas of interest within these plots. We conclude in Sect. 5.

## 2. Numerical setup

### 2.1. Equations and algorithm

We performed 2.5D simulations of fast-mode MHD waves that exhibited a realistic initial density profile (enhanced and depleted wave part) and interacted with low-density regions of different geometries that represented various possible shapes of CHs. In our simulation code, we use the MHD equations of continuity, momentum, and induction, including the standard notations for the variables,

$$\frac{\partial \rho}{\partial t} + \nabla \cdot (\rho \mathbf{v}) = 0, \quad (1)$$

$$\frac{\partial (\rho \mathbf{v})}{\partial t} + \nabla \cdot (\rho \mathbf{v} \mathbf{v}) - \mathbf{J} \times \mathbf{B} = 0, \quad (2)$$

$$\frac{\partial \mathbf{B}}{\partial t} - \nabla \times (\mathbf{v} \times \mathbf{B}) = 0. \quad (3)$$

We considered an idealized case with a background magnetic field that is homogeneous and zero pressure throughout the computational box. Therefore, no energy equation needs to be included in this setup.

The code we used to run the simulations was applied in several previous studies (e.g., Piantschitsch et al. 2017, 2018a,b, 2020, 2023). The code is based on the so-called total variation diminishing Lax-Friedrichs (TVDLF) method, which is a fully explicit scheme and was first described by Tóth & Odstrčil (1996). To numerically solve the standard MHD equations (see Eqs. (1)–(3)), we make use of an alternating direction implicit method (ADI), which allows us to apply the TVDLF method in each coordinate direction separately. By including the Hancock predictor method (van Leer 1984), we obtain second-order temporal and spatial accuracy. The Hancock predictor step is based on the idea that within our computational grid, we use first cell averages to predict the values of the conserved quantities at the cell edges in an auxiliary time step. Subsequently, the predicted values can be used to update the solution. A stable behaviour near discontinuities is guaranteed by applying the so-called Woodward limiter (for details, see van Leer 1977 and Tóth & Odstrčil 1996). To be able to also incorporate source terms in our scheme, we included a four-stage Runge-Kutta method in the code. For numerical reasons, the Runge-Kutta operator is split into two separate steps; the first step consists of one half of the time step and is applied before the TVDLF-operator, and the other step consists of the other half of the original Runge-Kutta time step, but is applied after the TVDLF operator.

We used Neumann boundary conditions at all four boundaries. In our simulation code, this means that the two rows of ghost cells at every boundary exhibit the same numerical value as those of the corresponding cell at the very edge of the actual computational grid. The size of the computational box is equal to 1.0 in the  $x$ - and  $y$ -direction. We performed the simulations using a resolution of  $300 \times 300$ .

## 2.2. Initial conditions

For the CW simulation, we applied two different initial conditions reflecting (1) a simple purely enhanced incoming wave pulse and (2) a more realistic profile. A realistic density profile here means a CW profile that includes an enhanced and a depleted wave part, as was observed in Muhr et al. (2011), for instance. In our simulations, we focused on CWs with an amplitude compression factor of about 1.1, which is typical for CWs with moderate speeds (Warmuth 2015).

The enhanced part of the initial incoming wave was excited in the following way:

$$\rho(x) = \begin{cases} \Delta\rho \cdot \cos^2\left(\pi \frac{x-x_0}{\Delta x}\right) + \rho_0 & 0.4 \leq x \leq 0.6, \\ 0.1 & x \geq 0.8, \\ 1.0 & \text{else,} \end{cases} \quad (4)$$

where  $\Delta\rho = 0.1$ ,  $x_0 = 0.5$ ,  $\Delta x = 0.2$ , and  $\rho_0 = 1.0$ . For the remaining variables,

$$v_x(x) = \begin{cases} 2 \cdot \sqrt{\frac{\rho(x)}{\rho_0}} - 2.0 & 0.4 \leq x \leq 0.6, \\ 0 & \text{else,} \end{cases} \quad (5)$$

$$B_z(x) = \begin{cases} \rho(x) & 0.4 \leq x \leq 0.6, \\ 1.0 & \text{else,} \end{cases} \quad (6)$$

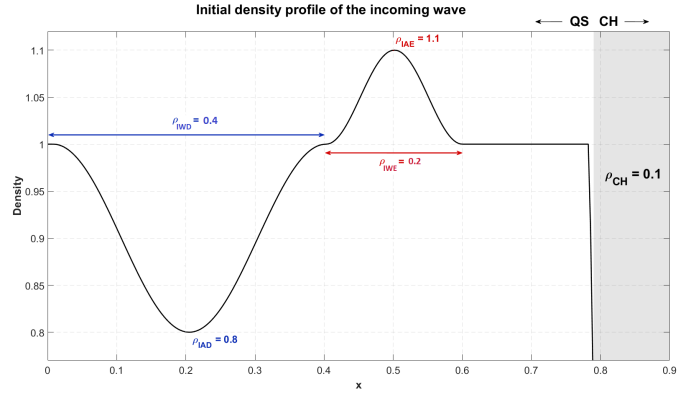


**Fig. 1.** Initial density profile of the incoming wave with a CH density of  $\rho_{\text{CH}} = 0.1$ . The sharp density drop represents the CHB. We chose  $\rho_{\text{IAE}} = 1.1$  for the initial enhanced amplitude (which corresponds to  $\Delta\rho = 0.1$ ,  $\rho_0 = 1.0$ , and  $x_0 = 0.5$  in Eq. (4)),  $\rho_{\text{IAD}} = 0.8$  for the initial depleted amplitude (which corresponds to  $\Delta\rho = -0.2$ ,  $\rho_0 = 1.0$ , and  $x_0 = 0.2$  in Eq. (4)),  $\rho_{\text{IWE}} = 0.2$  for the initial width of the enhanced part (which corresponds to  $\Delta x = 0.2$  in Eq. (4)), and  $\rho_{\text{IWD}} = 0.4$  for the initial width of the depleted wave part (which corresponds to  $\Delta x = 0.4$  in Eq. (4)).

$$B_x = B_y = 0, \quad 0 \leq x \leq 0.9, \quad (7)$$

$$v_y = v_z = 0, \quad 0 \leq x \leq 0.9. \quad (8)$$

The rear and depleted part of the incoming wave was excited in an analogous way simply by choosing  $\Delta\rho = -0.2$  and  $x_0 = 0.2$ . The range in which the density, the velocity, and the magnetic field values were defined was shifted to  $0 \leq x \leq 0.4$ . This particular excitation generated a wave in which the desired features only propagated toward the CH, that is, to the right in our coordinate system.

The results in Piantschitsch et al. (2023) showed that the strongest and most visible interaction effects are obtained by combining a sufficiently low CH density, an initial density profile for the incoming wave that includes an enhanced and a depleted part, and a sharp gradient representing the CHB width. We therefore used the following parameters as initial setup: The CH density was set to the value of  $\rho_{\text{CH}} = 0.1$ , the CHB was considered to be a step function (sharp gradient), and we used amplitude values of  $\rho_{\text{IAE}} = 1.1$  for the initial enhanced amplitude and  $\rho_{\text{IAD}} = 0.8$  for the depleted amplitude. We also defined  $\rho_{\text{IWE}} = 0.2$  to be the initial width of the enhanced part and  $\rho_{\text{IWD}} = 0.4$  to be the initial width of the depleted part. The incoming CW was invariant in the  $y$ -direction, that is, the CW was a superposition of plane waves with all their wave vectors parallel to the  $x$ -direction. In Fig. 1 we show the full density profile of the incoming wave, the CH density, and the density amplitudes and widths for the enhanced and depleted part of the initial incoming wave.

In our simulations, we focused on simple geometries, such as circular, elliptic, concave, and convex structures. This means that the CH geometries in the numerical setup were simulated in an idealized way, but still motivated by the shapes detected in the observations. Figure 2 shows different polar CHs that dominate the CH distribution at times of low solar activity (Cranmer 2009). Figure 3, on the other hand, shows CHs in the disk centre that typically are slightly smaller than the polar CHs. The examples of CHs in Figs. 2 and 3, which serve as a motivation for the choice of the CH structure in our simulations, do not exhibit perfect and simple geometrical shapes. However, every

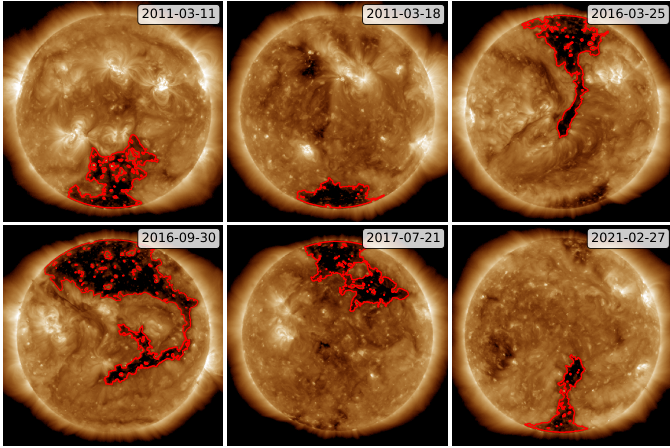


**Fig. 2.** Different polar CHs, which dominate the CH distribution at times of low solar activity, show longer convex and concave parts at their boundaries. CATCH (Heinemann et al. 2019) was used to detect the boundaries of these CHs, whose outline is marked in each panel by red curves. The background images were obtained with the Atmospheric Imager Assembly (AIA, Boerner et al. 2012; Lemen et al. 2012) on board the Solar Dynamics Observatory (SDO, Pesnell et al. 2012) in the 19.3 nm passband.

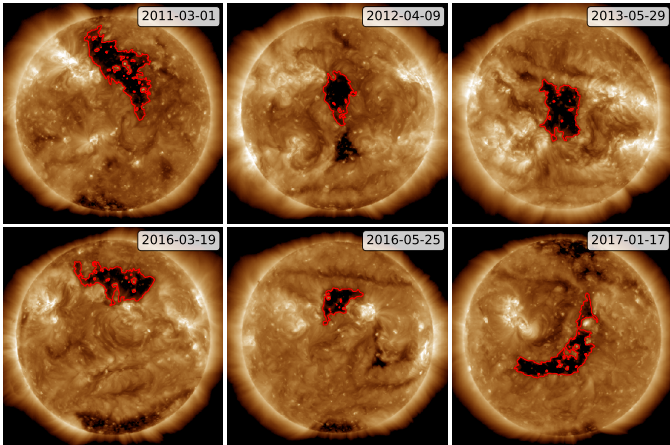


**Fig. 3.** Different CHs located in the disk centre. These CHs, which tend to appear in more active periods of the Sun, often exhibit circular or elliptical shapes or a combination of these basic geometries. CATCH (Heinemann et al. 2019) was used to detect the boundaries of these CHs, whose outline is marked in each panel by red curves. The background images were obtained with SDO/AIA in the 19.3 nm passband.

complex geometrical structure can be considered as a combination of simpler shapes, which explains our approach to first focus on idealised shapes before moving on to complex structures.

Figure 4 shows the different CH geometries we used in the initial setup of the simulations. We studied cases of so-called closed shapes, such as small circular and elliptical CHs, which represent CHs that are more likely to be found in the disk centre (see Figs. 4a–c). The larger low-density structures in Figs. 4d–f mostly represent polar CHs. For the case of a large concave shape, we considered the symmetric and the asymmetric situation (see Figs. 4e and f). We also compared the results obtained by a simulation including a realistic initial density profile with a situation in which the incoming wave was a purely enhanced pulse (see Fig. 4a).

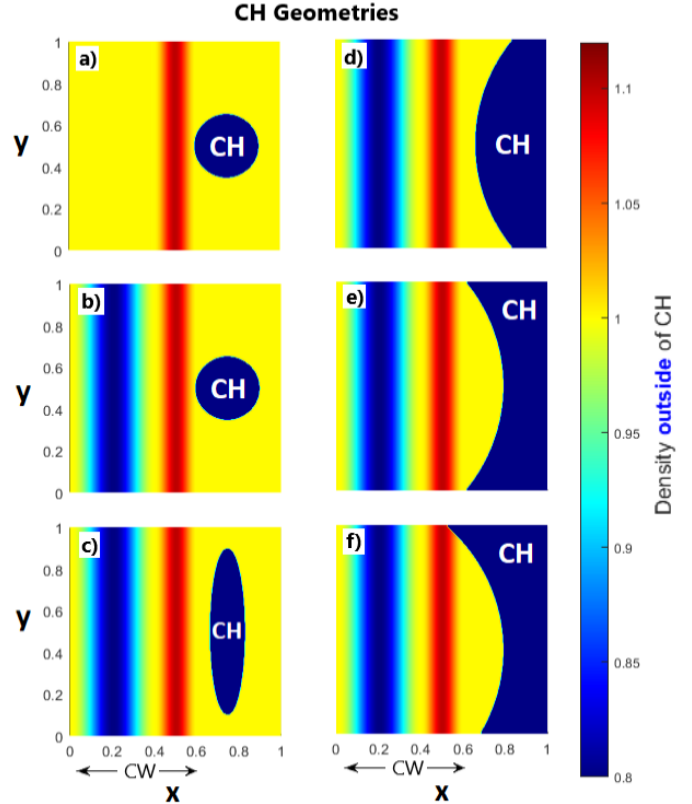


**Fig. 4.** Initial conditions for different CH geometries. Panel a shows an incoming wave that consists of a purely enhanced pulse (red) and a circular CH. Panel b again shows a circular CH, but with an incoming wave that combines an enhanced pulse (red) with a depletion region at the rear of the wave (blue). Panels c–f show incoming waves with enhanced as well as depleted parts and different CH shapes (elliptical in (c)), convex in (d), concave symmetric in (e), and concave asymmetric in (f). Panels a–c refer to small CHs, which are commonly found in the disk centre, and plots d–f refer to large CHs.

The time-distance plots that we used to analyse the properties of the incoming and reflected wave were created along three different paths within the computational box (see Path1, Path2, and Path3 in Fig. 5). In this way, we tried to address the fact that observational time-distance plots are commonly obtained by choosing one on several possible propagation slits (see e.g., Fig. 1 in Gopalswamy et al. 2009). Due to projection effects and the still rather low quality and accuracy of CW measurements, it can be quite challenging to choose the correct propagation direction in the observations. We tried to address this problem by choosing different paths along which the simulated time-distance plots were created, and we compared the different results.

### 3. Simulation results: 2D density structure

#### 3.1. Temporal evolution of the density structure

In this section, the temporal evolution of a straight incoming wave (i.e. the propagation direction at every point of the incoming wave is the positive  $x$ -direction) that interacts with CHs of different geometries is analysed, together with the corresponding time-distance plots and the density profiles of the incoming and reflected wave.

In Fig. 6 we show the temporal evolution of a CW that interacts with CHs of different shapes (circle, ellipse, convex, concave symmetric, and concave asymmetric). In the case of

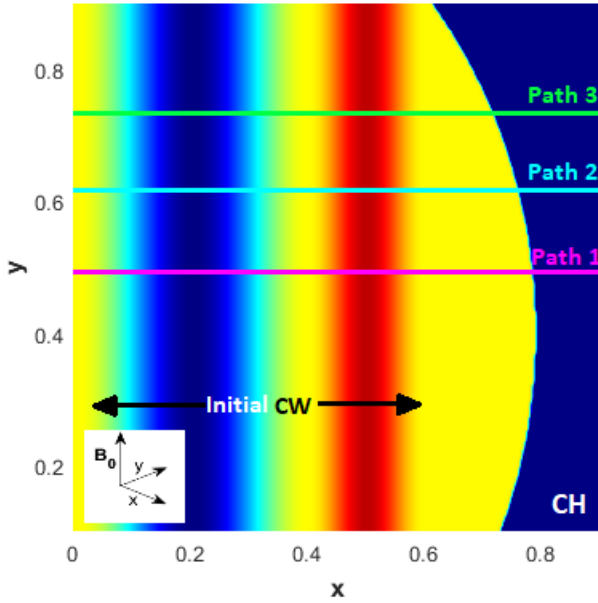


**Fig. 5.** Three different paths (Path1, Path2, and Path3) along which the time-distance plots were generated. The vertical dark blue structure at the left denotes the depleted part of the initial incoming wave, and the vertical red structure represents the enhanced part of the incoming wave (details of the amplitudes are shown in Fig. 1). The CH exhibits an asymmetric concave density structure and has a CH density of  $\rho_{\text{CH}} = 0.1$ . The background magnetic field is homogeneous and always points in the  $z$ -direction in this 2D setup.

a small circular CH, we analysed two situations. First, a setup that included a purely enhanced amplitude as an incoming wave (panel a in Fig. 6), and second, a setup that considered a realistic initial wave density profile (enhanced and depleted wave part) for the interaction with the CH (panel b in Fig. 6). This comparison between a purely enhanced and a realistic initial density profile is repeated in panels f and g, but in this case, including an asymmetric and concave CH. These direct comparisons between two different initial incoming waves show how significantly a realistic density profile changes the density distribution throughout the interaction process (for details, see Piantschitsch et al. 2023). Panels b–f, on the other hand, always use a realistic initial wave density profile, but compare the effects of the different CH shapes on the density distribution of the CW–CH interaction.

The results of the temporal evolution of the 2D density structure are given in Fig. 6 with a focus on the various CH shapes. In all different cases, an incoming wave interacts with CHs of different shapes. The incoming wave is reflected at the CHB and undergoes phase changes that eventually lead to superposition effects, that is, there is an interplay between the constructive and destructive interference of the reflected and incoming wave parts (cf. Fig. 10 in Piantschitsch et al. 2023). In the case of a realistic initial wave density profile (Figs. 6b–f), this is especially interesting because the interaction between the already reflected part of the enhanced incoming wave and the still incoming depleted part of the incoming wave leads to large depleted density areas and to a time period during which no wave part reaches values above the background density (see  $t_3$  in panels d–f). Subsequently, when the depleted part of the incoming wave starts to interact with the CH and hence starts to enter a phase-changing process as well, the depleted amplitude of the reflected wave again starts to exhibit higher density values (still below the background density, however). Eventually, one part of the reflected

wave is pushed towards the background density level until it reaches amplitude values above the background density level. These phase changes of the enhanced and depleted incoming wave part, combined with the corresponding effects of constructive and destructive interference that are intensified or reduced depending on the CH shape, lead to quite different density structures (see  $t_5$  from (a)–(g)).

A comparison between panels a and b, but also between panels f and g, shows that an interaction that includes a realistic initial density profile leads to higher reflected density values (see the red structures in  $t_5$ ) and to an almost entirely depleted density structure in the middle of the interaction process (see  $t_3$ ; for details regarding this comparison, see Piantschitsch et al. 2023). Depending on the CH geometry, the effects of high reflected density values and depleted areas are more or less pronounced. While small and closed CHs (circular and elliptic) lead to quite small reflected density amplitudes, the large concave and convex CH structures exhibit much stronger interaction effects. The dark red structures at  $t_5$  in panels e and f show that the reflected density amplitude can obtain values even higher than the initial incoming density amplitude, and the depleted area in the middle of the interaction process reaches values far lower than the initial incoming depleted wave part. As we show below, when we analyse the density profiles in detail in Sect. 4, the reflected density amplitude in the asymmetric concave case is able to reach values even twice higher than the values of the incoming density amplitude. In Table 1 we list the minimum and maximum density values within the reflected wave for the different CH shapes shown in Fig. 6. The highest but also the lowest density value during the interaction process is obtained by the asymmetric concave CH ( $\rho_{\text{max}} \approx 1.24$  and  $\rho_{\text{min}} \approx 0.73$ ), whereas the weakest interaction effects are a result of the interaction with a small circular CH ( $\rho_{\text{max}} \approx 1.06$  and  $\rho_{\text{min}} \approx 0.78$ ). As already mentioned above, all these different density values occur due to the interplay between the constructive and destructive interference of the different reflected and incoming wave parts.

Piantschitsch et al. (2023) showed that large reflected density amplitudes can be obtained by combining a sufficiently low CH density with a small incident angle and a realistic initial wave density profile, including an enhanced and depleted part. (Here, the incident angle is defined as the angle that the wave vector forms with the CHB.) When even only one of these three conditions is not satisfied, no large reflected density amplitude can be reached. This result is again confirmed in Fig. 6f, which shows that a concave CH with a low CH density leads to quite strong interaction effects. However, these high density values are not obtained in panel g, in which the incoming wave is considered to be a purely enhanced pulse. In other words, a purely enhanced incoming wave is sufficient to significantly reduce the strong interaction effects seen in panel f. This once again shows the importance of the correct choice for the initial wave profile in MHD simulations that include CWs.

### 3.2. Representative incident angles

The question now is how the different high- and low-density values within the reflected part of the wave can be explained. In other words, whether more details about the effects of constructive and destructive interference of the reflected wave parts for the different CH shapes are known. Piantschitsch & Terradas (2021) have provided analytical expressions for three representative incident angles that yield information about the phase of the reflected wave and also about whether transmission occurs through the CH. All of these angles only depend on the density

Temporal evolution of the 2D density structure  
for different CH shapes

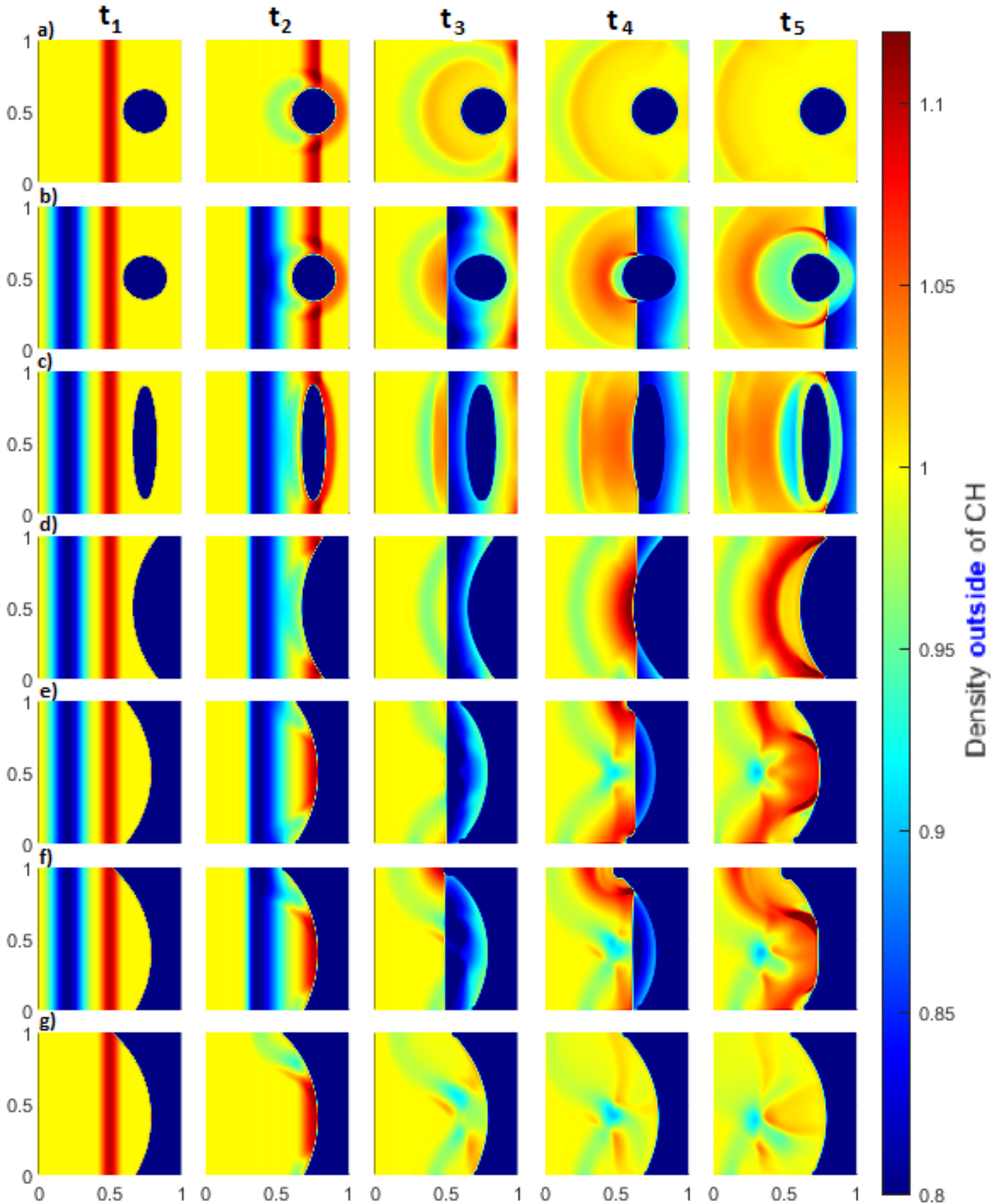


**Fig. 6.** Temporal evolution of the density distribution of a straight incoming wave that interacts with CHs of different shapes. (a) Interaction of a wave that consists of a purely enhanced pulse with a circular CH. (b) Circular CH and a CW that includes a density enhancement at the wave front and a depletion region in the rear part of the incoming wave. (c) Elliptical CH. (d) Symmetric convex CH. (e) Symmetric concave CH. (f) Asymmetric concave CH. (g) Purely enhanced pulse with an asymmetric concave CH.

contrast  $\rho_c$  (ratio of the CH density to the density of the quiet Sun), which is equal to the CH density in our case because we considered the background density to be equal to 1.0. The first angle in this list of representative incident angles is the so-called critical angle,  $\theta_C$ ,

$$\theta_C = \cos^{-1}(\sqrt{\rho_c}). \quad (9)$$

This angle separates the situation of a full reflection from a situation that includes transmission, that is, incident angles above the critical angle lead to transmitted waves, whereas incident angles below the critical angle result in pure reflections (for details, see Figs. 7 and 8 in [Piantschitsch & Terradas 2021](#)).

The second representative angle is the so-called Brewster angle,  $\theta_B$ ,

$$\theta_B = \cos^{-1}\left(\sqrt{\frac{\rho_c}{1+\rho_c}}\right), \quad (10)$$

and it represents a situation in which perfect transmission takes place, that is, there is no reflection at the CHB at all. The third important incident angle that separates enhanced from depleted reflection is the so-called phase-inversion angle,  $\theta_P$ ,

$$\theta_P = \cos^{-1}\left(\sqrt{\frac{\rho_c + \rho_c^2}{1 + \rho_c^2}}\right), \quad (11)$$

where  $\rho_c$  again denotes the density contrast. For linear waves, this implies that an enhanced incoming wave with an incident angle between the Brewster angle and the phase-inversion angle is reflected as an enhanced wave, whereas incoming waves that exhibit an incident angle outside of this range undergo a phase change and propagate as depleted reflections. For a CH density of  $\rho_{CH} = 0.1$ , for instance, we know that the Brewster angle,  $\theta_B$ , is equal to  $72.5^\circ$ , the phase inversion angle,  $\theta_P$ , is equal to  $70.8^\circ$ , and the critical angle,  $\theta_C$ , is equal to  $71.6^\circ$ . For a low CH density, these values are very close to each other. This means that a small change in the incident angle is already sufficient to turn a case of full transmission into a case of no transmission at all. This result provides crucial information for the interpretation of CW–CH interaction effects in observational data. Table 2 shows these transmission features and the phase characteristics for a general incident angle and provides values for the three different representative angles in the case of  $\rho_{CH} = 0.1$  (for more details, see [Piantschitsch & Terradas 2021](#)). We emphasize that the analytical expressions for the representative angles and the corresponding phase characteristics were derived using linear wave theory. However, we are interested in linear and weakly non-linear MHD waves here (up to a compression factor of 1.1), which are also motivated by observational measurements of CWs ([Mühr et al. 2011](#); [Warmuth 2015](#)). These theoretical results therefore seem to be a sufficiently reasonable basis for interpreting the simulation results.

A situation that considers an interaction with a concave CH includes many different incident angles and therefore leads to a superposition of reflected waves that exhibit different phases and amplitudes. Table 2 shows that probably all four different incident angles are involved in the case of a concave CH. This means that some incoming enhanced wave parts might be reflected as depletions, some might be reflected as enhanced waves, some might be fully reflected, and some might travel through the CH too (and analogously for the depleted incoming wave part). Moreover, the representative angles always depend on the CH density, and therefore, the density structure of an interaction

**Table 1.** Minimum and maximum density values of the reflected wave after the interaction with different CH shapes (circle, ellipse, convex, concave symmetric, and concave asymmetric), considering an initial incoming wave profile with  $\rho_{IAE} = 1.1$  for the initial enhanced amplitude,  $\rho_{IAD} = 0.8$  for the depleted amplitude,  $\rho_{IWE} = 0.2$  for the initial width of the enhanced part, and  $\rho_{IWD} = 0.4$  for the initial width of the depleted part.

CH shape	$\rho_{\max}$ of reflection	$\rho_{\min}$ of reflection
Circle	$\approx 1.06$	$\approx 0.78$
Ellipse	$\approx 1.07$	$\approx 0.76$
Convex	$\approx 1.13$	$\approx 0.74$
Concave symm.	$\approx 1.2$	$\approx 0.74$
Concave asymm.	$\approx 1.24$	$\approx 0.73$

with a concave CH can look very different depending on the CH density. These considerations show how complex the interaction process can be, depending on the CH geometry, the CH density, and the initial incoming density profile.

## 4. Simulation results: Time-distance plots

### 4.1. Time-distance plots depending on CH geometry

The temporal evolution of the incoming and reflected density profiles can be studied in more detail by analysing the corresponding line profiles and time-distance plots. In Fig. 7, we show the three different paths (at  $t = 0$  and  $t = 520$ ) along which the line profiles and the time-distance plots were created. We decided to choose different paths to analyse the density profiles because in the observations, it is often difficult to choose a clear and unambiguous slit for generating time-distance plots. The propagation direction in the observations is usually not sufficiently clear and unequivocal for determining a unique propagation direction. We therefore used different paths to generate the line profiles in the MHD simulations and thus to capture the different propagation directions in the observations.

Figure 7a shows a 3D visualisation of the initial setup including the initial incoming wave with a realistic density profile and an asymmetric concave area of low density that denotes the CH. Plot b shows the initial 2D density distribution of the simulation setup ( $t = 0$ ). Plot c shows the density distribution at  $t = 520$ . Plots d–f of Fig. 7 show the time-distance plots that were created along the three different paths. The blue and green areas denote regions in which the density is below the background density, whereas the red and orange areas denote regions in which the density is larger than the background density. The dark blue regions denote the CH. The vertical black lines in Figs. 7d–f refer to the same density profiles as the corresponding paths in Fig. 7c. This plot clearly shows that the density structure in the time-distance plots varies depending on the path we use to create it, that is, the time-distance plot corresponding to Path 1 shows stronger interaction effects than the time-distance plot based on Path 3.

Figures 8 and 9 show the time-distance plots that correspond to the temporal evolution of the density distribution in Fig. 6. Figure 8 shows the time-distance plots for the circular and elliptical CH. Panels a–c show the situation of a purely enhanced incoming wave in combination with a circular CH. Here, the enhanced reflected part (dark orange structure pointing into the lower right corner of the plot) is barely visible, as in the density structure of Fig. 6a. Panels d–f depict the time-distance plots of



**Table 2.** Representative angles, transmission features, and phase characteristics for general incident angles and for the case of  $\rho_{CH} = 0.1$ .

	Incident angle general	Incident angle for $\rho_{CH} = 0.1$	Phase characteristics
TRANSM.	$\rho_B < \rho_I < 90^\circ$	$72.5^\circ < \rho_I < 90^\circ$	<b>Enhan.</b> Incom. → <b>Deplet.</b> Reflect.
	$\rho_I = \rho_B$	$\rho_I = 72.5^\circ$	Full transmission
	$\rho_I < \rho_I < \rho_B$	$71.6^\circ < \rho_I < 72.5^\circ$	<b>Enhan.</b> Incom. → <b>Enhan.</b> Reflect.
NO TRANS.	$\rho_P < \rho_I < \rho_C$	$70.8^\circ < \rho_I < 71.6^\circ$	<b>Enhan.</b> Incom. → <b>Enhan.</b> Reflect.
	$0^\circ < \rho_I < \rho_P$	$0^\circ < \rho_I < 70.8^\circ$	<b>Enhan.</b> Incom. → <b>Deplet.</b> Reflect.

**Notes.** For a CH density of  $\rho_{CH} = 0.1$ , the Brewster angle,  $\theta_B$ , is equal to  $72.5^\circ$ , the phase inversion angle,  $\theta_P$ , is equal to  $70.8^\circ$ , and the critical angle,  $\theta_C$ , is equal to  $71.6^\circ$ . One can see that incident angles above the Critical angle lead to transmitted waves whereas incident angles below the Critical angle result in pure reflection. The Brewster angle  $\theta_B$  represents a situation of perfect transmission, and the Phase inversion angle  $\theta_P$  separates enhanced from depleted reflection. For linear waves this implies that an enhanced incoming wave with an incident angle between the Brewster angle and the Phase inversion angle gets reflected as an enhanced wave, whereas incoming waves that exhibit an incident angle outside of this range undergo a phase change and propagate as depleted reflections.

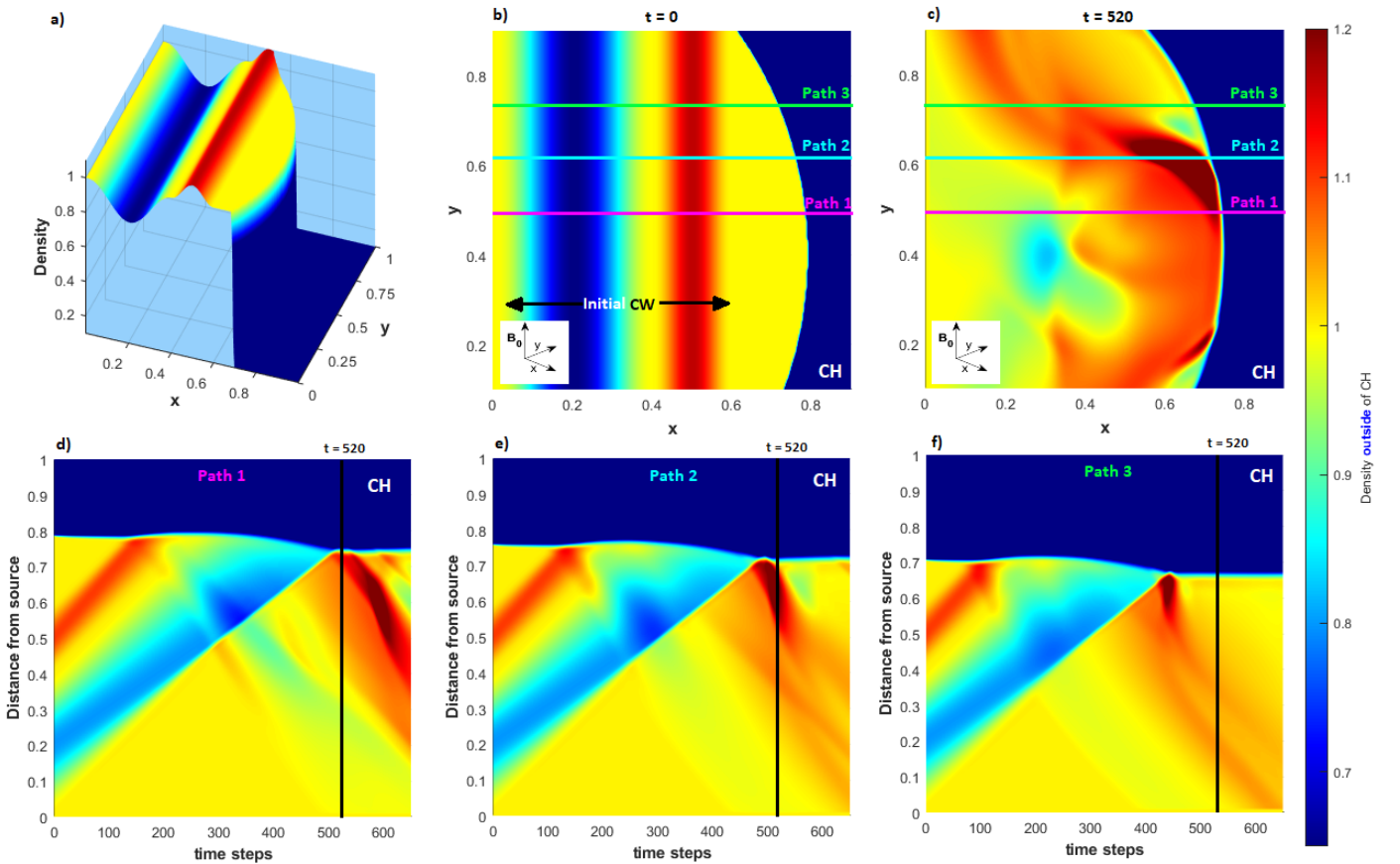


**Fig. 7.** Density structure of a CW that interacts with a concave CH and the corresponding time-distance plots based on three different paths. (a) 3D visualisation of the initial conditions of a straight incoming wave (including a density enhancement, red, and a depleted wave part, blue) that interacts with an asymmetric low-density concave area that denotes the CH. (b) 2D initial conditions at  $t = 0$ , as in plot a. The magenta, turquoise, and green lines denote the paths along which the different time-distance plots are generated. (c) Density distribution at the end of the temporal evolution ( $t = 650$ ) of the CW–CH interaction, together with the three paths along which the time-distance plots are created. (d)–(f) Time-distance plots showing the temporal evolution of the incoming and reflected wave along Path 1 (magenta), Path 2 (turquoise), and Path 3 (green). The blue and green areas denote regions in which the density is lower than the background density, and the red and orange areas denote regions in which the density is higher than the background density.

the interaction between an incoming wave including a realistic initial density profile and a circular CH, and panels g–i show this interaction with an elliptical CH. As shown in Fig. 6b and c, there is a region around time step  $t = 200$  in which only density values lower than the background density are detected (blue and light green areas). No regions like this are visible in the situation of the purely enhanced incoming wave in Fig. 6a.

Another result that was also already visible in the temporal evolution of Fig. 6 is the fact that along all three different paths (for the realistic initial density profile), the width of the enhanced reflected wave is broader than that of the incoming wave. However, in none of the situations is the (enhanced) reflected amplitude larger than the incoming amplitude. The larger width of the reflected enhanced wave part can be explained by the large width

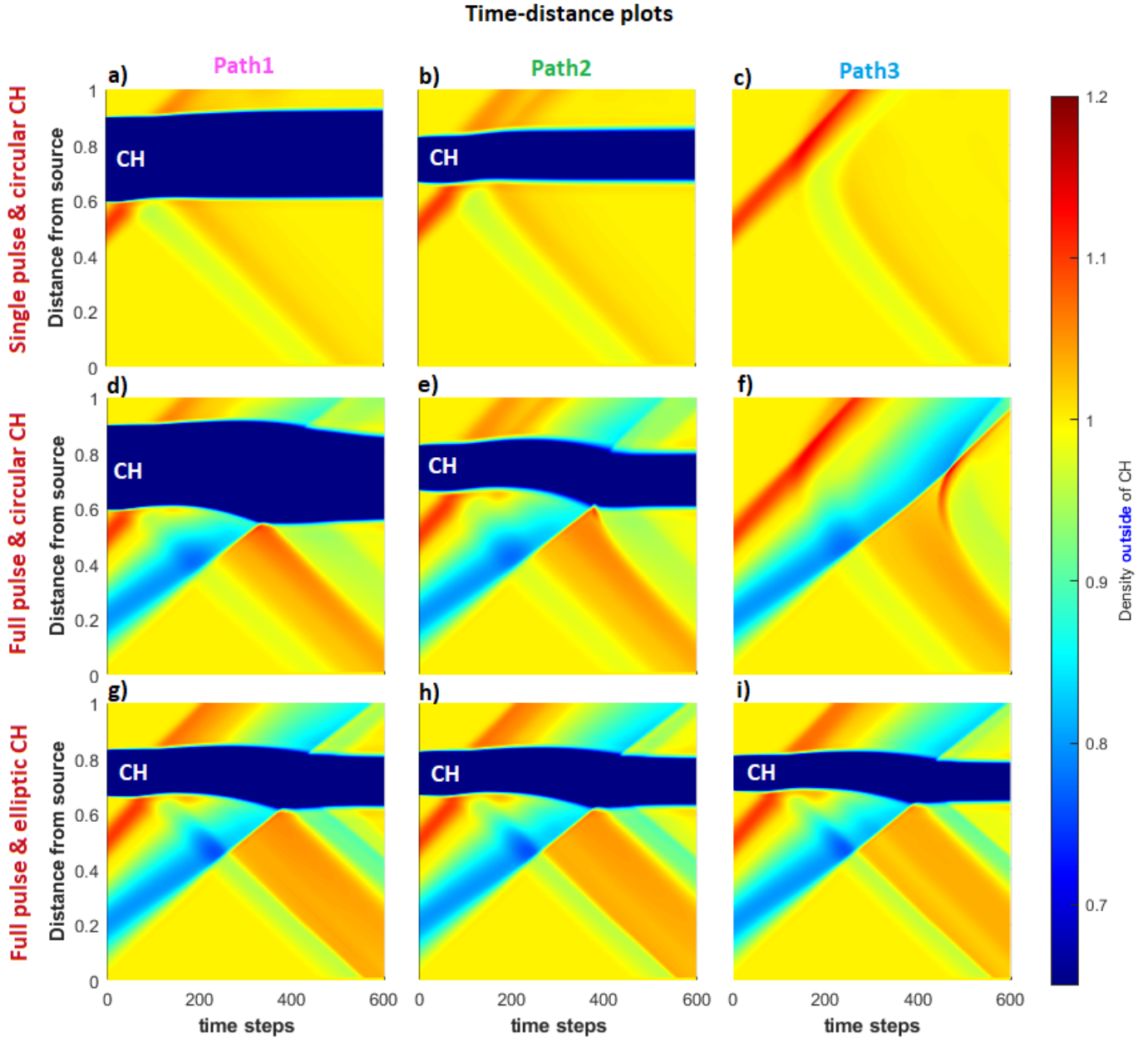


**Fig. 8.** Time-distance plots along Path1 (magenta), Path2 (green), and Path3 (blue) for different density profiles of the incoming wave and different CH geometries. The blue and green regions denote areas in which the density is lower than the background density (depletion), and the red and orange regions denote areas in which the density is higher than the background density (enhancement). The horizontal dark blue regions denote the CH area. (a)–(c): Time-distance plots of an incoming wave that only consists of an enhancement without a depletion in the rear part of the wave that interacts with a circular CH. (d)–(f): Time-distance plots of an incoming wave with a density profile consisting of an enhancement at the wave front and a depletion area in the rear part of the wave that interacts with a circular CH. (g)–(i): Time-distance plots of a full density profile (enhancement + depletion) that interacts with an elliptic CH and a CH density of  $\rho_{\text{CH}} = 0.1$ .

of the initial depleted part of the incoming wave. The density amplitudes of the reflected wave, which are smaller than those of the incoming wave in this case, can be explained by the shapes of the CHs, which do not lead to sufficiently strong effects of constructive interference of the different reflected wave parts. Within the density structure of panels d–i, a small bump is visible that points into the direction of the upper left part of the plots. This bump, which continues into the direction of the green and yellow area, depicts the motion of the first reflected wave part that travels through the still incoming rear part of the wave until it reaches (due to destructive interference effects) the lowest interaction density values. It finally propagates as a slightly depleted

reflection (light green structure below the enhanced reflection) away from the CH.

Figure 9 shows the time-distance plots for a convex, a symmetrical concave, and an asymmetrical concave CH. Similar to the cases of a small circular and elliptical CH, the interaction with a convex CH does not result in a larger enhanced reflected amplitude than the incoming amplitude. The situation for a concave CH is different, however, as shown in panels d–i of Fig. 9. The time-distance plots for the symmetric and the asymmetric concave CH show a dark red area within the enhanced reflected wave part. Here, the reflected amplitude is more than twice larger than the incoming amplitude. Moreover,

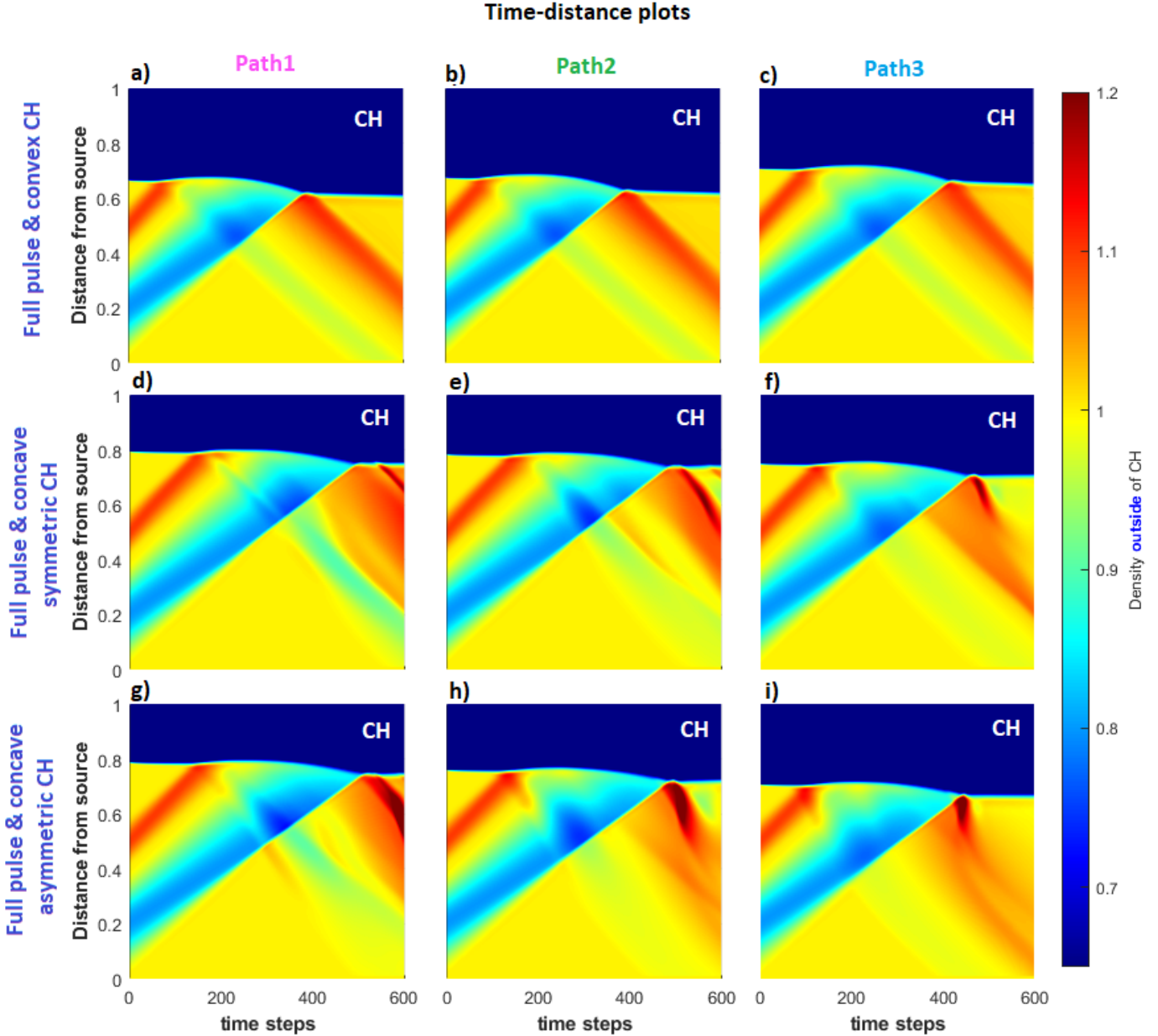


**Fig. 9.** Time-distance plots along Path1 (magenta), Path2 (green), and Path3 (blue) for different density profiles of the incoming wave and different CH geometries. The blue and green regions denote areas in which the density is lower than the background density (depletion), and the red and orange regions denote areas in which the density is higher than the background density (enhancement). The horizontal dark blue regions denote the CH area. All incoming waves consist of an enhancement at the wave front and a depletion area in the rear part of the wave. The CH density for all cases is  $\rho_{\text{CH}} = 0.1$ . (a)–(c): Interaction with a convex CH. (d)–(f): Interaction with a concave symmetric CH. (g)–(i): Interaction with a concave asymmetric CH.

especially in the asymmetric concave case (g)–(i), the angle of the reflected wave is different from that of the incoming wave, it is more strongly bent towards the centre of the time-distance plot. The large reflected amplitude structure (dark red structure) is caused by constructive interference effects when the incoming wave interacts with a concave shape. Generally, these effects of constructive and destructive interference cause the density structure of the reflected wave to appear to be much more complex in the concave case than in all other cases. In addition to the non-uniform density structure of the enhanced reflected part, the depleted part, which moves ahead within the reflected wave, also shows a different behaviour than in the other cases (see (d)–(i)). Neither the enhanced nor the depleted reflection exhibit a uni-

form width or amplitude while moving away from the CH. This makes it challenging to determine a clear propagation direction in the simulations as well as in the observations.

In observations, the reflected phase speed is typically derived by drawing a line along the presumed direction of the reflected wave in the time-distance plots (in our simulations, this is the dark red structure). When the angle formed by the direction of the incoming wave and a vertical line is larger than the angle formed by the direction of the reflected wave and a vertical line (see e.g. Fig. 7), we interpret the reflected phase speed to be higher than the incoming speed. This method is only valid when the actual incoming propagation direction is the same as the reflected one, however, which is usually not the case. This

means that when we use the same path to generate the time-distance plots of the incoming and the reflected wave, we have to be very careful. In the concave case, the dark red region in Fig. 6f (which is the large enhanced amplitude of the reflected wave) moves across the computational box. However, it does not only move in the negative  $x$ -direction, but even points into the upper left corner of the computational box. This creates the bent dark red structure in the corresponding time-distance plots. Moreover, it is dangerous in this case to try to obtain the reflected phase speed by drawing a straight line because this does not reflect the actual situation of the interaction process. The bent structure in the time-distance plots provides more information about a change in the propagation direction of the reflected wave than about the actual phase speed. However, we can rely on the value of the large reflected amplitude. This result also shows that it is important to choose a correct path to create time-distance plots.

In Fig. 10 we analyse the temporal evolution of the density profile for the central magenta path in case of the asymmetric concave CH in more detail. Panel a shows the initial density profile, and panel b shows that the incoming wave propagates towards the CH, which is also shown along the vertical green line in the time-distance plot at the bottom. Panel c shows that the incoming wave propagates towards the CH and is about to interact with the CHB. In panel d, the interaction has just begun and a first part of the wave enters the CH, while another part of the wave front is reflected at the CHB, undergoing a phase change. In panel f of Fig. 10, the front part of the incoming wave was reflected already (see the blue arrows in panel f and the time-distance plot at the bottom) and interacts with the still incoming rear (depleted) part of the initial wave. This also explains that in panel f, no density value higher than the background density is visible. The same is true for the line profiles in panels h and i, where the low-density values are also visible as blue and green structures in the time-distance plot. Panel l already shows reflected density values that are clearly much higher than the initial density amplitude of the incoming wave. Panel m shows that after the entire incoming wave has interacted with the CHB, the amplitude of the reflection is able to reach a value more than twice higher than the initial enhanced amplitude of the incoming wave. This large amplitude is also visible in the time-distance plot at the bottom of the figure, denoted along the turquoise vertical line. Panel h and in the time-distance plot below, in which the vertical pink line is located, show that the density amplitude reaches a value below the initial depleted density amplitude of the incoming wave. This is the result of the destructive interference between the depleted part of the reflection and the still incoming depleted wave part.

#### 4.2. Representative interaction features in the time-distance plots

The final goal we aim to achieve with the help of the parameter studies in this paper is a comparison of the simulation results to actual observed interaction events. This motivated us to already determine specific regions within the simulation-based time-distance plots that exhibit characteristic density features that can then be directly compared to observational time-distance plots. Based on this, we aim to derive, in a further step, interaction parameters from the observed interaction events that usually cannot be obtained directly from the measurements. Figure 11 shows that we divided the density structure of the time-distance plot into different regions of interest. The black rectangle denotes

the part of the interaction in which the entire incoming wave still moves towards the CH until shortly before the front part of the wave starts to interact with the CHB. The inclined red structure within this black rectangle denotes the enhanced part of the incoming wave, and the blue and green areas denote the depleted part that follows the wave front during the propagation towards the CH. The area enclosed by the magenta rectangle shows the density structure in the time period during which no density value above background density level can be detected. Within this rectangle, some reflected wave part tries to push the rear part of the incoming wave backwards (dashed white line). This is the reflected (depleted) part of the enhanced incoming wave that moves through the depleted still incoming wave part in the negative  $x$ -direction. After the first reflected part has completed travelling through the still incoming depletion, it continues to travel in the negative  $x$ -direction and is now visible as the light orange area (see also the dashed black line). The black circle within the magenta rectangle denotes the area in which the density structure reaches its minimum value. It is located at the position where the lowest density value of the first reflected part of the incoming wave meets the lowest density values of the still incoming depletion. Hence, the interference leads to the lowest density value of the entire interaction process. The region enclosed by the white rectangle denotes the area in which the reflected wave mostly travels as a depletion in the negative  $x$ -direction and none of the strongly enhanced reflected wave parts are visible so far. The area that is enclosed by the green rectangle represents the region in which the reflected wave is again visible as an enhanced wave. In this area, the wave reaches values higher than the background density everywhere, and in some parts, it even reaches density values higher than twice those of the incoming wave (dark red area). This high-density region starts to appear at the time when the rear part of the incoming wave has completely entered the CH, and it is the result of the superposition of several different wave components that propagate towards the central part of the computational box. We recall that this interference is only possible due to the concave geometry of the CH. In all other cases, the reflected waves cannot reach higher density values than the incoming waves. In Fig. 11 we also defined two directions for the incoming and reflected wave (white arrows). They are commonly defined in the observational time-distance plots in this way. The simulation results show, however, that time-distance plots have to be used with caution to analyse incoming and reflected waves. Using only one slit may lead to incorrect conclusions regarding the reflected phase speed. This figure also clearly shows the deformation of the CH boundary due to the incoming wave. This deformation has not been investigated in detail from the observational point of view so far. However, it will be included in the direct comparison to an actual observed event in our follow-up study.

## 5. Conclusions

We performed the first MHD simulations of CWs that interact with CHs with different geometries. The initial simulation setup was based on the results of Piantschitsch et al. (2023), where we analysed the effects of a CW density profile with an enhanced and a depleted wave part on the CW-CH interaction process. In this paper, we focused on the shape of the CHs by considering different basic geometries, such as circular, elliptical, convex and concave density structures. We analysed the density profiles of the incoming and reflected waves as well as the temporal evolution of the 2D density structure during the whole interaction process. Moreover, we generated the corresponding time-distance

## Temporal evolution of line profiles compared to time distance plot

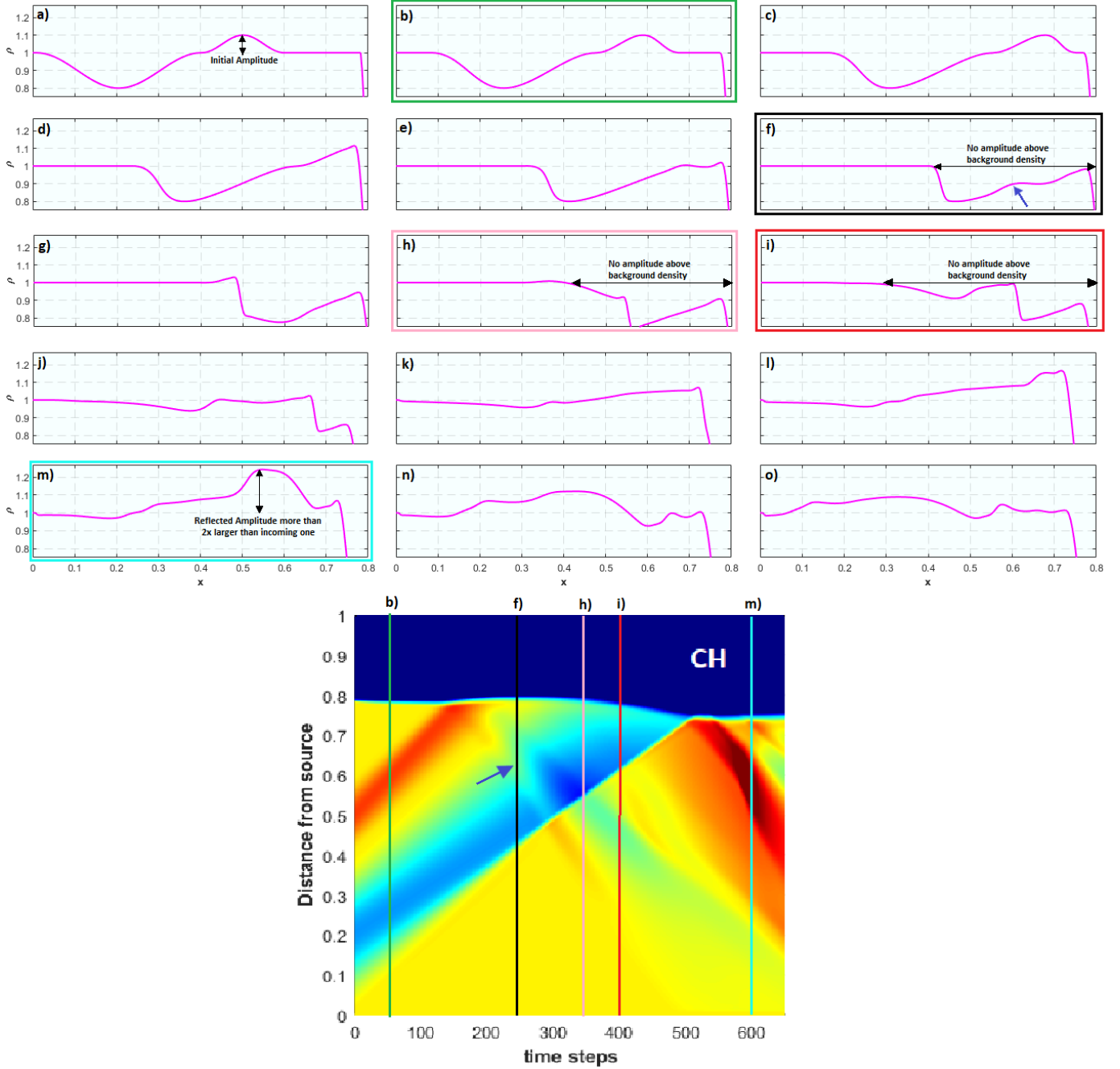


**Fig. 10.** Temporal evolution of the density wave profile (incoming and reflected wave) along Path1 (magenta) compared to the related time-distance plot of this interaction with a concave asymmetric CH. Panel a shows the initial density profile with an enhanced amplitude of  $\rho_{\text{Ampl}} = 1.1$  and a CH density of  $\rho_{\text{CH}} = 0.1$ . Plot b is also represented as vertical green line in the time-distance plot at the bottom and shows that the incoming wave still moves towards the CH. Panel b shows that no part of the density profile reaches a value higher than the background density  $\rho_0 = 1.0$ . A similar situation is shown in panels h and i. These profiles are denoted in the time-distance plot as vertical black, pink, and red lines. The temporal evolution between panels e and j clearly shows that the first reflected wave part propagates through the depleted part of the incoming wave. Panel m shows that the amplitude of the reflected wave is able to reach a value that is more than twice higher than the density amplitude of the incoming wave. This large amplitude is also shown as the dark red structure in the time-distance plot below.

plots, and within these plots, we determined specific regions that exhibit characteristic density features that in a further step will be compared to actual observed CW-CH interaction events.

The main results are summarised below.

1. For the first time, simulations of the interaction between CHs of various shapes and CWs that include an enhanced
2. as well as a depleted part were performed. Depending on the shape of the CH, differences in the interaction effects, such as large reflected density amplitudes and entirely depleted areas within the density structure, were detected (see Fig. 6).

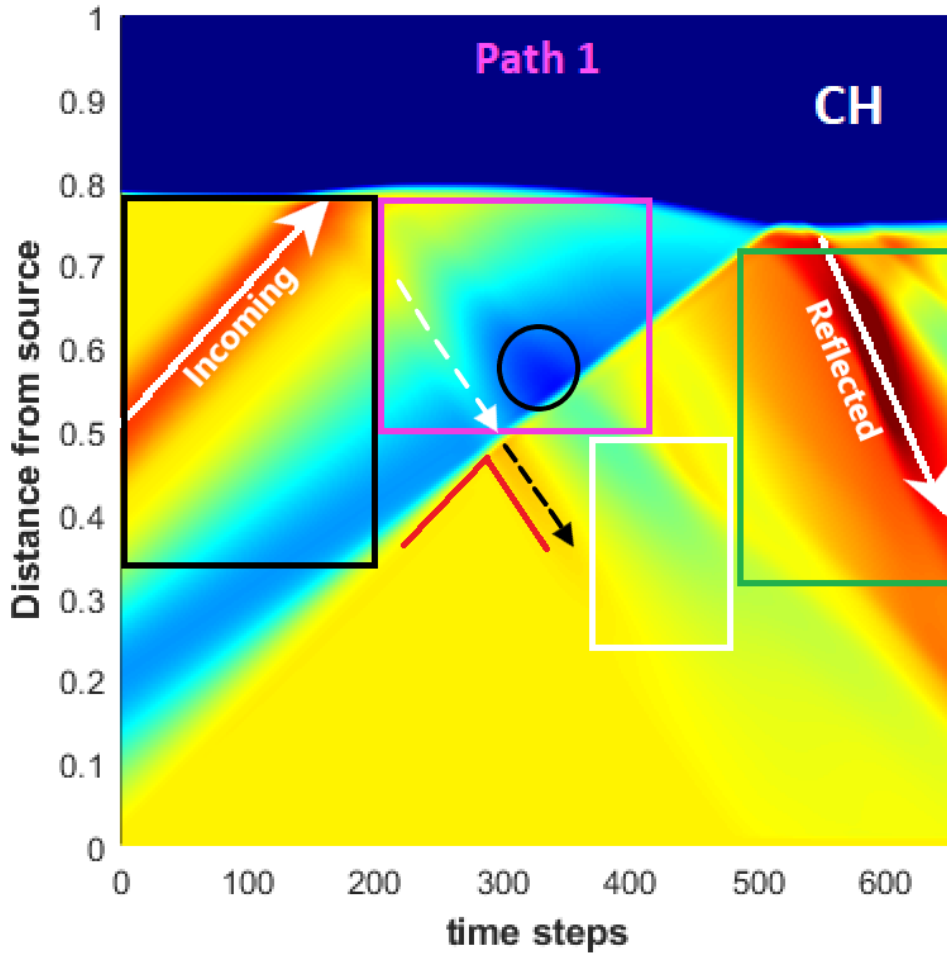


**Fig. 11.** Time-distance plot of the interaction between an incoming wave including a realistic density profile (enhancement + depletion) and an asymmetric concave CH with a CH density of  $\rho_{\text{CH}} = 0.1$  and an initial density amplitude of  $\rho_{\text{IAP}} = 1.1$ , created along the central path (Path1, magenta). The black rectangle denotes the area in which the incoming wave moves towards the CH and no interaction has taken place so far. The magenta rectangle shows the part of the interaction in which no density value higher than the background density level can be detected, and the black circle within the magenta rectangle denotes the area in which the density structure reaches its minimum value. The area that is enclosed by the green rectangle represents the region in which the reflected wave can be seen as an enhanced wave again, always reaching values higher than the background density and even reaching density values more than twice those of the incoming wave (dark red area). The white rectangle denotes the area where the reflected wave mostly travels as a depletion and none of the strong enhanced reflected wave parts is visible so far. The dashed white and black lines denote the paths of a first reflection that travels through the rear part of the still incoming wave.

with a concave CH led to higher reflected density amplitudes than the incoming density amplitudes (see Figs. 8 and 9). Effects of constructive interference between different reflected wave parts in combination with a low CH density and the realistic initial wave density profile enable the reflected density amplitudes to reach values that are more than twice higher than the initial density amplitude of the incoming wave (see e.g. the dark red structure in Figs. 10, 11, and Table 1).

3. Only the interaction with a concave CH leads to a significantly larger reflected density amplitude. However, the shape of the CH is not sufficient to reach high-density values like this. Only in combination with a realistic initial density profile (enhancement + depletion) and a small CH density can strong interaction effects like this be obtained. If even only one of these conditions is not satisfied, no large reflected density amplitudes can be reached (see Fig. 6).
4. Another feature that is caused by interference effects of the reflected and the incoming wave is a strongly depleted region in the middle of the CW-CH interaction process. While a first part of the incoming wave is already reflected and starts

to undergo a phase change, the rear part of the incoming (depleted) wave still moves towards the CHB. The interference of the two depleted wave parts (reflected and incoming) leads to a depleted area that exhibits lower density values than the initial depletion amplitude of the incoming wave (see e.g. the dark blue structure in Figs. 10 and 11). This also implies that for some time period during the interaction process, no wave part is visible above the background density. This is an important information for the analysis of reflected waves in observations.

5. The time-distance plots in this study show that there is not only one single reflected wave, but several different reflected wave parts. The enhanced reflection is usually visible in observations, which exhibits a clear and strong enhanced amplitude. However, the simulations show that an incoming wave that includes a realistic density profile causes several different (depleted and enhanced) reflections that together cause complex superposition effects within the density structure of the interaction process (see the distribution into different regions of interest in Fig. 11).

6. The different CH geometries lead to complex interference effects within the time-distance plots of the interaction process. These effects, on the one hand, can be explained by the different paths that were chosen to create these plots. On the other hand, depending on the CH density, it is possible to derive three representative incident angles, the Brewster angle, the critical angle, and the phase-inversion angle (see Eqs. (9)–(11)), which provide information about the transmission features and the phase characteristics of the reflected waves (see Table 2). These properties also partially explain the interplay between the constructive and destructive interference of the involved wave parts (for more details, see [Piantschitsch & Terradas 2021](#)).
7. By identifying and analysing different density areas within the simulation-based time-distance plots (see Fig. 11), we will be able to directly compare these areas and their density features to the density structure of observational time-distance plots. This will also enable us to derive interaction parameters from the observed interaction events that typically cannot be obtained directly from the measurements.

We are aware that the shapes of realistic CHs are much more complex, which probably leads to different properties than are shown on the time-distance maps. This will be addressed in detail in a future study. As a next step, in the follow-up study to this paper, the simulation results obtained in this current paper in combination with the results from [Piantschitsch et al. \(2023\)](#) will be used to partially reconstruct an actual observed CW–CH interaction event. We emphasize that in this theoretical study, we were interested in linear and weakly non-linear CWs with a compression factor of about 1.1 or lower, which was motivated by intensity measurements of CWs in observations ([Muhre et al. 2011](#)). The interaction results are expected to change for interactions that include strongly non-linear waves that lead to the evolution of shocks and other features.

We recall that the simulation setup we used is still idealised, including zero gas pressure and a homogeneous background magnetic field in the  $z$ -direction. In future studies, we plan to implement a more realistic magnetic field structure that includes curved magnetic field lines at the CHB and a stratified atmosphere to be able to study vertical effects at different heights and their effect on the properties of the secondary waves. The 2D models developed in [Terradas et al. \(2022\)](#), [Terradas \(2023\)](#) might be useful for these purposes. We also point out that we used a specific inclination angle for the convex and concave shapes of the CHs. Different choices of these inclination angles might influence the intensity of the interaction effects.

In addition to the properties of the reflected wave, the transmission coefficient and its relation to the reflection coefficient is another important topic. The detailed properties of the transmitted wave for the different CH shapes are beyond the scope of this study, but will be addressed in future studies. However, we would like to mention that in [Piantschitsch et al. \(2020\)](#) and [Piantschitsch & Terradas \(2021\)](#), we have published theoretical results regarding the properties of the transmitted wave during

a CW–CH interaction event and the relation of the transmission coefficient to the reflection coefficient.

*Acknowledgements.* This research was funded by the Austrian Science Fund (FWF): Erwin-Schrödinger fellowship J4624-N. For the purpose of Open Access, the author has applied a CC BY public copyright licence to any Author Accepted Manuscript (AAM) version arising from this submission. This work was supported by the Austrian Science Fund (FWF): I3955-N27. JT and RS acknowledge support from the R+D+i project PID2020-112791GB-I00, financed by MCIN/AEI/10.13039/501100011033. SGH acknowledges funding by the Austrian Science Fund (FWF): Erwin-Schrödinger fellowship J-4560. The SDO/AIA data are available courtesy of NASA/SDO and the AIA science teams.

## References

- Afanasyev, A. N., & Zhukov, A. N. 2018, *A&A*, 614, A139  
 Boerner, P., Edwards, C., Lemen, J., et al. 2012, *Sol. Phys.*, 275, 41  
 Chandra, R., Chen, P. F., Devi, P., Joshi, R., & Ni, Y. W. 2022, *Galaxies*, 10, 58  
 Cranmer, S. R. 2009, *Liv. Rev. Sol. Phys.*, 6, 3  
 Delaboudinière, J. P., Artzner, G. E., Brunaud, J., et al. 1995, *Sol. Phys.*, 162, 291  
 Del Zanna, G., & Bromage, B. J. I. 1999, *J. Geophys. Res.*, 104, 9753  
 Del Zanna, G., & Mason, H. E. 2018, *Liv. Rev. Sol. Phys.*, 15, 5  
 Domingo, V., Fleck, B., & Poland, A. I. 1995, *Space. Sci. Rev.*, 72, 81  
 Gopalswamy, N., Yashiro, S., Temmer, M., et al. 2009, *ApJ*, 691, L123  
 Heinemann, S. G., Temmer, M., Heinemann, N., et al. 2019, *Sol. Phys.*, 294, 144  
 Heinemann, S. G., Jerčić, V., Temmer, M., et al. 2020, *A&A*, 638, A68  
 Heinemann, S. G., Saqri, J., Veronig, A. M., Hofmeister, S. J., & Temmer, M. 2021, *Sol. Phys.*, 296, 18  
 Hofmeister, S. J., Asvestari, E., Guo, J., et al. 2022, *A&A*, 659, A190  
 Jarolim, R., Veronig, A. M., Hofmeister, S., et al. 2021, *A&A*, 652, A13  
 Kienreich, I. W., Muhr, N., Veronig, A. M., et al. 2013, *Sol. Phys.*, 286, 201  
 Lemen, J. R., Title, A. M., Akin, D. J., et al. 2012, *Sol. Phys.*, 275, 17  
 Linker, J. A., Heinemann, S. G., Temmer, M., et al. 2021, *ApJ*, 918, 21  
 Liu, R., Wang, Y., Lee, J., & Shen, C. 2019, *ApJ*, 870, 15  
 Long, D. M., Gallagher, P. T., McAtteer, R. T. J., & Bloomfield, D. S. 2008, *ApJ*, 680, L81  
 Mancuso, S., Bemporad, A., Frassati, F., et al. 2021, *A&A*, 651, L14  
 Moreton, G. E., & Ramsey, H. E. 1960, *PASP*, 72, 357  
 Muhr, N., Veronig, A. M., Kienreich, I. W., Temmer, M., & Vršnak, B. 2011, *ApJ*, 739, 89  
 Olmedo, O., Vourlidas, A., Zhang, J., & Cheng, X. 2012, *ApJ*, 756, 143  
 Pesnell, W. D., Thompson, B. J., & Chamberlin, P. C. 2012, *Sol. Phys.*, 275, 3  
 Piantschitsch, I., & Terradas, J. 2021, *A&A*, 651, A67  
 Piantschitsch, I., Vršnak, B., Hanslmeier, A., et al. 2017, *ApJ*, 850, 88  
 Piantschitsch, I., Vršnak, B., Hanslmeier, A., et al. 2018a, *ApJ*, 857, 130  
 Piantschitsch, I., Vršnak, B., Hanslmeier, A., et al. 2018b, *ApJ*, 860, 24  
 Piantschitsch, I., Terradas, J., & Temmer, M. 2020, *A&A*, 641, A21  
 Piantschitsch, I., Terradas, J., Soubrie, E., et al. 2023, *A&A*, 679, A136  
 Podladchikova, T., Veronig, A. M., Podladchikova, O., et al. 2019, *EGU General Assembly Conference Abstracts*, 9793  
 Reiss, M. A., Muglach, K., Möstl, C., et al. 2021, *ApJ*, 913, 28  
 Riley, P., Linker, J. A., & Arge, C. N. 2015, *Space Weather*, 13, 154  
 Samara, E., Magdalenic, J., Rodriguez, L., et al. 2022, *A&A*, 662, A68  
 Saqri, J., Veronig, A. M., Heinemann, S. G., et al. 2020, *Sol. Phys.*, 295, 6  
 Terradas, J. 2023, *Physics*, 5, 276  
 Terradas, J., Soler, R., Oliver, R., et al. 2022, *A&A*, 660, A136  
 Thompson, B. J., Plunkett, S. P., Gurman, J. B., et al. 1998, *Geophys. Res. Lett.*, 25, 2465  
 Tóth, G., & Odstrčil, D. 1996, *J. Comput. Phys.*, 128, 82  
 van Leer, B. 1977, *J. Comput. Phys.*, 23, 276  
 van Leer, B. 1984, *SIAM J. Scien. Stat. Comput.*, 5, 1  
 Veronig, A. M., Temmer, M., Vršnak, B., & Thalmann, J. K. 2006, *ApJ*, 647, 1466  
 Vršnak, B., & Lulić, S. 2000, *Sol. Phys.*, 196, 157  
 Warmuth, A. 2015, *Liv. Rev. Sol. Phys.*, 12, 3  
 Zhou, X., Shen, Y., Tang, Z., et al. 2022, *A&A*, 659, A164